Broadband suppression of laser intensity noise based on second-harmonic generation

Y. Li,[1,*] F. Seddighi,[1] and G. Porat[1,2]

[1] *Department of Electrical and Computer Engineering, University of Alberta, Edmonton, Alberta T6G 2R3, Canada*
[2] *Department of Physics, University of Alberta, Edmonton, Alberta T6G 2E1, Canada*

(Received 5 March 2024; revised 13 May 2024; accepted 6 June 2024; published 11 July 2024)

We present a novel method for the suppression of laser intensity noise and pulse-to-pulse energy fluctuation, based on second-harmonic generation. This method is broadband, passive, has low complexity, and suppresses noise uniformly over the noise spectrum. We theoretically model, analytically analyze, and numerically simulate this technique's performance for cw and nanosecond pulse lasers with different pulse shapes. We demonstrate broadband relative intensity noise suppression of up to 48 dB, and pulse-to-pulse energy fluctuation suppression of up to 50 dB, and highlight the significance of these findings for extending atom trap storage time, e.g., for quantum information processing.

DOI: 10.1103/PhysRevApplied.22.014026

I. INTRODUCTION

Laser intensity noise is a hindrance for many established and emerging applications, such as microscopy [1], high-precision interferometry [2], spectroscopy [3], and particularly atom trapping [4–9] for quantum simulation and quantum information processing, where a contribution to loss rate is directly proportional to the trapping laser relative intensity noise (RIN) spectral density, thereby strongly motivating the development of methods for intensity noise reduction.

Established methods of laser intensity noise attenuation generally fall into two categories: pump power modulation or downstream light modulation via acousto-optic modulation (AOM) or electro-optic modulation (EOM). Both approaches rely on tapping the laser output to generate an electrical signal for feedback control systems that drive the pump power or light modulation such that it counteracts intensity fluctuations [10,11]. Pump power modulation achieves a noise-suppression bandwidth of up to about 1 MHz. This approach is limited to diode-pumped lasers with fast diode current control electronics. Recently, it was extended by also injecting the laser output into a saturated semiconductor optical amplifier and filtering its amplified spontaneous emission, achieving a noise-suppression bandwidth of 50 MHz [12]. Unfortunately, this approach strongly limits the output laser power to the amplifier's saturation point. Noise suppression via downstream AOM is limited to sub-MHz frequencies by the bandwidth of the modulator. Bulk EOM has been shown to facilitate noise suppression up to 10 MHz [13], while waveguide EOM reaches multi-GHz noise suppression bandwidths [14]. However, both EOM cases involve significant limitations. Bulk EOM requires high half-wave voltages (100–1000 V), which introduces complexity and cannot be driven faster than a few MHz. Waveguide EOM has a low damage threshold, supporting laser powers only much less than 1 W. In both cases, operation depends crucially on the laser's mean power level (e.g., due to saturation of electronics), necessitating manual adjustments of the feedback system whenever laser power is changed (e.g., due to long-term drift or aging). A recent experiment utilized AOM for its excellent performance at dc–10 kHz, combined with an EOM for 10 kHz–1 MHz, where the EOM requires only a small dynamic range that is easy to manage with high frequencies [11]. This highly complex approach achieved a 15-dB suppression of noise spectral power density up to 1 MHz, where optimal operation is accompanied by a transmission of 50%, increasing the atom trap lifetime by a factor of 10. All these feedback-based approaches introduce significant complexity. Even within their bandwidth, the degree of noise suppression can vary by orders of magnitude depending on noise frequency. Additionally, any such feedback system inevitably increases noise at some range of frequencies beyond its bandwidth (colloquially called "servo bump" or "bode bump") [15].

Past approaches that utilize nonlinear wave mixing for noise suppression relied on saturating optical parametric amplifiers (OPAs) [16], nonlinear polarization rotation (NPR) [17], or intracavity second-harmonic generation (SHG) [18–20]. While OPA saturation achieves 15-dB

*Contact author: yishen3@ualberta.ca

noise suppression over a bandwidth of 10 GHz, it is a very complex approach, requiring additional pump lasers and many fiber components. Because noise suppression via NPR utilizes an interferometric configuration of similar complexity, it also requires very good mechanical stability. Furthermore, it is practically applicable only to femtosecond pulses with sufficiently high peak intensity to drive the weak Kerr effect that facilitates NPR. Just a 4-dB reduction in pulse-to-pulse energy fluctuation has been demonstrated with this method. Intracavity SHG works as a weak nonlinear loss mechanism that supplements laser gain saturation to counteract intensity fluctuation due to relaxation oscillation, reducing RIN by up to 6 dB at GHz frequencies. However, this highly complex approach requires special laser design and is extremely difficult to implement for existing lasers. Recently, a brief note was published on rms RIN suppression with phase-mismatched extracavity SHG [21], with no investigation of the physical mechanism underlying this anecdotal observation.

To overcome the complexity and limitations of existing techniques, here we present a method of passive noise attenuation based on single-pass extracavity phase-matched SHG. For clarity, we emphasize that this method does not change the laser's optical frequency but rather suppresses noise at the fundamental frequency. This method is simple to implement and has nearly infinite bandwidth since it relies on a perturbative light-matter interaction with subfemtosecond response time. For the same reason, it provides the same degree of noise attenuation regardless of noise frequency.

Since our method is based on a nonlinear optical process, its performance depends on laser intensity in the SHG crystal and on the amount of intensity noise. Below we analyze this dependence for cw and various pulsed lasers. We show that in optimal conditions and where the laser initial rms RIN is low, rms RIN suppression reaches at least 24 dB, corresponding to 48-dB attenuation of RIN spectral density. Even when initial rms RIN is as high as 10%, rms RIN is attenuated by 13 dB (i.e., RIN spectral density attenuation of 26 dB). Therefore, when applied to trapping beams, this method can increase atom trap storage time by orders of magnitude, and even eliminate intensity noise as a significant contributing factor to trap loss rate. Additionally, for pulsed lasers, we show that pulse-to-pulse energy fluctuation is suppressed by 50 dB.

II. THEORY

A. Fundamental wave transmission through second-harmonic generation

The SHG process is a special case of three-wave mixing with exact analytical solutions in the plane-wave approximation [22,23]. If the process is phase-matched and there is no second-harmonic light at the beginning of the interaction, the output intensity at the fundamental frequency is given by

$$I_{\omega,\mathrm{out}} = I_{\omega,\mathrm{in}}\mathrm{sech}^2\left(\sqrt{\zeta' I_{\omega,\mathrm{in}}}\right), \tag{1}$$

where

$$\zeta' \equiv \left(\frac{\sqrt{2}\omega d_{\mathrm{eff}} L}{n_1 (c^3 n_2 \epsilon_0)^{1/2}}\right)^2, \tag{2}$$

ω is the frequency of the fundamental wave, $I_{\omega,\mathrm{in}}$ is its initial intensity, n_1 and n_2 are the refractive indices of the fundamental and second-harmonic waves, respectively, d_{eff} is the second-order nonlinear coefficient of the medium, L is the length of the medium, c is the speed of light, and ϵ_0 is the permittivity of free space. We label this quantity ζ' to distinguish it from the commonly used parameter $\zeta \equiv 2\omega d_{\mathrm{eff}}|A_1(0)|L/(n_1 n_2)^{1/2}c$. We define a unitless normalized input intensity $\zeta' I_{\omega,\mathrm{in}}$, which contains both the nonlinear medium's properties and the input light intensity $I_{\omega,\mathrm{in}}$, making all discussions universally applicable to any nonlinear media.

Here, we wish to pay particular attention to the critical points of $I_{\omega,\mathrm{out}}$ as $I_{\omega,\mathrm{in}}$ changes. As we limit our discussion to the fundamental frequency (where the analysis of second-harmonic RIN can be found elsewhere [24]), the subscript ω is omitted hereon for brevity. Figure 1(a) shows the output intensity as a function of normalized intensity, which has a single maximum at $\zeta' I_{\mathrm{in}} = 1.43923$. Correspondingly, the derivative of I_{out} with respect to I_{in} crosses zero at the same point, as shown in Fig. 1(b). The reason for this trend can be understood as follows. Consider a given nonlinear medium, i.e., fixed ζ', so that the horizontal axis of Fig. 1(a) is proportional to input intensity. As the input intensity increases, the nonlinear transmission of the fundamental $T_{\mathrm{nl}} = I_{\mathrm{out}}/I_{\mathrm{in}}$ decreases, since a greater fraction of the input light gets converted to the second harmonic [see Fig. 2(b)]. While the input intensity increases linearly by definition, the transmission decreases nonlinearly as prescribed by Eq. (1). The product of these two opposing trends, which vary at different rates with input intensity, produces the maximum shown in Fig. 1(a). The critical value of $\zeta' I_{\mathrm{in}} = 1.43923$ is obtained by numerically finding the zero crossing of the analytical expression for the derivative,

$$\frac{dI_{\mathrm{out}}}{dI_{\mathrm{in}}} = \left(1 - \sqrt{\zeta' I_{\mathrm{in}}}\tanh\left(\sqrt{\zeta' I_{\mathrm{in}}}\right)\right)\mathrm{sech}^2\left(\sqrt{\zeta' I_{\mathrm{in}}}\right). \tag{3}$$

The maximum of I_{out} bears the physical significance that, if the input intensity I_{in} fluctuates around $\zeta' I_{\mathrm{in}} = 1.43923$, the nonlinear transmission of the medium would counteract the input intensity fluctuation, effectively suppressing the output intensity fluctuations. Consequently, this lays the basis for a nonlinear device that passively attenuates intensity noise.

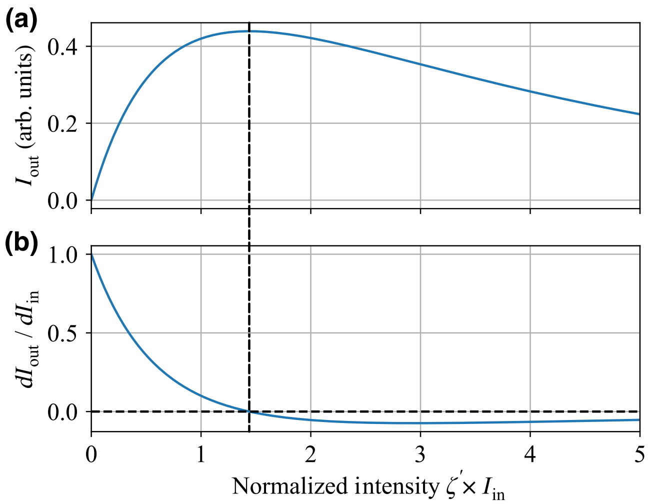

FIG. 1. (a) Output intensity and (b) its derivative with respect to input intensity, as functions of the normalized input intensity $\zeta' I_{in}$. The dashed lines indicate the critical point $\zeta' I_{in} = 1.43923$, where the output intensity reaches a maximum and its derivative vanishes.

B. Relative intensity noise (RIN)

For clarity, we first rigorously define the concepts of frequency-resolved RIN and rms RIN (also called integrated RIN). To distinguish the two quantities, we label them $\mathcal{R}_f$ and $\mathcal{R}_{rms}$, respectively, as both of these terms are commonly referred to simply as "RIN" in different publications. We begin by writing the intensity as

$$I(t) = \bar{I} + \delta I(t), \tag{4}$$

where $\bar{I}$ is the average intensity and $\delta I(t)$ is the time-dependent intensity noise. Then we have the following definitions [25]:

$$\mathcal{R}_f \equiv \frac{1}{\bar{I}^2} S_I(f), \tag{5a}$$

$$\mathcal{R}_{rms} \equiv \sqrt{\frac{1}{\bar{I}^2} \int S_I(f) df}, \tag{5b}$$

where f is noise frequency and $S_I(f)$ is the power spectral density of intensity noise. Here we carry out analysis in the time domain, where the statistical variance of $\delta I(t)$ is directly related to its power spectral density through $\sigma_I^2 = \int S_I(f)\, df$ [25], so that

$$\mathcal{R}_{rms} = \sqrt{\frac{\sigma_I^2}{\bar{I}^2}} = \left|\frac{\sigma_I}{\bar{I}}\right|, \tag{6}$$

and σ_I is the rms value of intensity noise. To evaluate noise attenuation performance, we consider the ratio of output and input $\mathcal{R}_{rms}$ as the $\mathcal{R}_{rms}$ transfer,

$$\mathcal{R}_{rms} \text{ transfer} \equiv \frac{\mathcal{R}_{rms,out}}{\mathcal{R}_{rms,in}} = \frac{\sigma_{I,out}/\bar{I}_{out}}{\sigma_{I,in}/\bar{I}_{in}}, \tag{7}$$

and similarly for $\mathcal{R}_f$. Below we show that the $\mathcal{R}_f$ transfer is independent of frequency. Therefore, by virtue of Eq. (5), the value of the $\mathcal{R}_f$ transfer is obtained by simply squaring the value of the $\mathcal{R}_{rms}$ transfer. For instance, a $\mathcal{R}_{rms}$ transfer of 10^{-1} (-10 dB) equates to 10^{-2} (-20 dB) $\mathcal{R}_f$ transfer.

C. First-order perturbation analysis

In this section, we assume the input intensity noise represents a small perturbation atop of the time-averaged intensity, i.e., $\delta I_{in}(t) \ll \bar{I}_{in}$. This is a common situation for many lasers, and it also alludes to analytical analysis that reveals insights into the noise attenuation process. To relate to our discussion on RIN statistics, let the standard deviation of $\delta I_{in}(t)$ be $\sigma_{I,in}$. Applying first-order Taylor expansion to Eq. (1), we write the fundamental output intensity as

$$I_{out}(t) = \bar{I}_{in} \mathrm{sech}^2\left(\sqrt{\zeta' \bar{I}_{in}}\right) + \delta I_{in}(t) \times \frac{dI_{out}}{dI_{in}}. \tag{8}$$

Similarly, we propagate the noise statistics to the first order by [26]

$$\sigma_{I,out} = \sigma_{I,in} \times \frac{dI_{out}}{dI_{in}}. \tag{9}$$

Using the definition of $\mathcal{R}_{rms}$ transfer in Eq. (7) and the expression for the derivative in Eq. (3), one finds

$$\mathcal{R}_{rms} \text{ transfer} = \left|1 - \sqrt{\zeta' \bar{I}_{in}} \tanh\left(\sqrt{\zeta' \bar{I}_{in}}\right)\right|. \tag{10}$$

Notice that the transfer of RIN depends solely on the average input intensity $\bar{I}_{in}$ for a given medium described by ζ', and it is thus independent of any frequency dependence of the input noise, thereby facilitating broadband noise attenuation. Additionally, when evaluated numerically, this function takes the range of 0 to 1 when $0 \leq \zeta' \bar{I}_{in} < 4.26562$. Figures 2(a) and 2(b) show the $\mathcal{R}_{rms}$ transfer as a function of normalized intensity and the corresponding intensity-dependent nonlinear transmission, respectively. The shaded region indicates the noise attenuation regime, and the nonlinear transmission at the point of zero noise transfer is 0.305, corresponding to a second-harmonic conversion efficiency of 0.695. These plots imply that a careful selection of the nonlinear medium and laser focusing geometry is necessary to avoid unintended noise amplification where $\zeta' \bar{I}_{in} \geq 4.26562$. However, because the nonlinear transmission is very low ($T_{nl} < 0.07$) in the noise amplification regime, it is anyway of low practical interest.

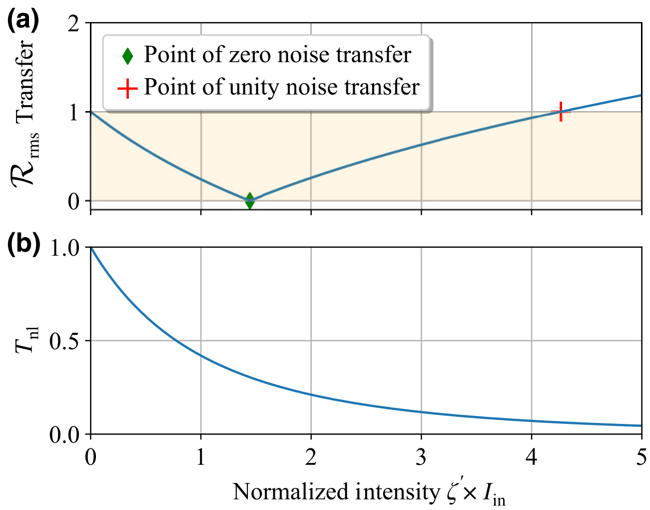

FIG. 2. (a) Perturbative $\mathcal{R}_{\rm rms}$ transfer as in Eq. (10) and (b) nonlinear transmission $T_{\rm nl}$ as a function of normalized intensity $\zeta' I_{\rm in}$.

III. NUMERICAL SIMULATION

In this section, we present numerical simulation results, for both cw and cases of pulsed lasers. Due to the time independence of the noise transfer function in Eq. (10), we may employ the same analysis for pulsed lasers, where we assume long pulses with an optical bandwidth much narrower than the SHG phase-matching bandwidth. In practice, this limits our analysis to pulse duration on the scale of nanoseconds or longer. For the sake of illustration, we will exemplify the noise attenuation process with a commonly used nonlinear crystal: periodically poled magnesium-oxide-doped lithium niobate (MgO:PPLN) with a length of 1 cm, quasi-phase-matched for the SHG of 1064 nm, which is the wavelength of the Nd:YAG laser commonly used in atom traps. Using the relevant Sellmeier equation [27], one finds that in this case $\zeta' = 7.68 \times 10^{-11}$ m^2/W, which will be assumed in the following simulations without compromising generality. To put this number in a practical perspective, the optimal input intensity corresponding to 1 cm of MgO:PPLN crystal is 1.9 MW/cm^2, which is below its cw laser-induced damage threshold [28]. In terms of power, a peak power of 300 W for a beam with 0.1-mm radius is required to reach the ideal intensity, a value that is easily accessible for nearly all nanosecond laser systems (e.g., 3-μJ pulse energy with 10-ns pulse duration).

Interestingly, a recent experiment investigated RIN in the second harmonic generated from a cw laser with 1064-nm wavelength [24]. A model for RIN transfer into the second harmonic was developed, along the same lines as here, using perturbative noise and the analytical solution for the plane-wave approximation. The RIN transfer model and experiment presented in Ref. [24] showed excellent agreement when the fundamental beam was focused into a 30-mm long lithium tantalate crystal with a radius of 48 μm, where the confocal length is about the same as the crystal length. Therefore, the plane-wave model correctly predicts experimental measurements of second-harmonic RIN even under focusing conditions at the edge of its validity range. This encourages using intensity values corresponding to similar focusing conditions in our plane-wave numerical investigation of the RIN of the fundamental wave.

For the 1-cm-long MgO:PPLN crystal considered in this work, the same focusing condition implies a beam radius of 27 μm. Optimal noise suppression of the output fundamental beam would then require an input power of 22 W. Therefore, for cw lasers, the scheme presented here is applicable to somewhat high power, though this requirement can be relaxed by using longer crystals (since $\zeta' \propto L^2$), in combination with schemes that increase effective crystal length such as multicrystal SHG [29], multipass SHG [30], or cavity-enhanced SHG [31]. For example, the single-pass power requirement for cw lasers could be lowered to 4.6 W by focusing into a 5-cm MgO:PPLN crystal with 64-μm beam radius. As another example, the four single-pass configuration of Devi *et al.* [29] with 5-cm-long MgO:PPLN crystals and a 64 microns beam radius, further reduces the optimal power by a factor of 16 to 288 mW. To extend the application of this technique to cw lasers with even lower emission power, such as milliwatt-level midinfrared interband cascade lasers with exquisite spectral properties [32], it may not be possible to avoid the added complexity of amplification [33,34] to reach the optimal power for noise attenuation. In this proposed scheme, noise suppression needs to more than compensate for potential noise degradation by amplification to deliver an overall benefit (though some amplification schemes can even reduce noise [16]).

To present the noise-attenuation results progressively, we organize this section as follows: we start by considering RIN attenuation for a cw laser. Next, we examine RIN attenuation for various pulsed sources with Gaussian and super-Gaussian intensity profiles, for which we also calculate the attenuation of pulse-to-pulse fluence fluctuations. Finally, we characterize both intensity and fluence noise in pulses with asymmetrical shapes.

The numerical simulations in this section use randomly generated numbers with given RIN statistics to represent intensity or fluence noise as white noise with a prescribed rms value. The implementation and data visualization of numerical studies utilizes numpy and matpotlib [35,36]. We choose an rms value of 10^{-1} to represent the most extreme nonperturbative value of practical interest for input RIN, and 10^{-5} to represent the perturbative noise limit without any hindrance of generality, as results are very similar when the rms value is even 100 times greater. The latter range covers the noise properties of most lasers.

A. Continuous wave

We start by examining the simplest case of continuous waves. Figure 3 shows the $\mathcal{R}_{\mathrm{rms}}$ transfer for the perturbative case, calculated both numerically and analytically with Eq. (10), and the numerical calculation for the nonperturbative case. For ease of reference, the corresponding nonlinear transmission is indicated at the top of the plot. For perturbative noise (10^{-5}), the analytical and numerical results agree on optimal rms noise attenuation greater than 250 (48-dB $\mathcal{R}_f$ attenuation). In fact, the analytical expression gives rise to an exact zero noise transfer (to first order) when the intensity equates to its critical point. The numerical result at the critical point becomes lower as the numerical resolution of the normalized intensity improves. This implies that a better agreement with the analytical result of greater RIN attenuation is numerically demonstrable, although here it is limited by our numerical precision. Figure 3 also includes the $\mathcal{R}_{\mathrm{rms}}$ transfer for $\mathcal{R}_{\mathrm{in}} = 10^{-3}$, which is essentially the same as for $\mathcal{R}_{\mathrm{in}} = 10^{-5}$, showing the extent of the perturbative regime. For nonperturbative noise (10^{-1}), the rms RIN is nevertheless attenuated by more than 20 when $\zeta' I_{\mathrm{in}} = 1.43923$, corresponding to a 26-dB attenuation of $\mathcal{R}_f$. We emphasize that in all cases the optimal RIN attenuation significantly exceeds the nonlinear loss of optical intensity, as indicated by the nonlinear transmission of $T_{\mathrm{nl}} = 0.305$. In other words, the loss of noise power is much greater than the loss of average power, rendering the trade-off worthy. This is particularly true for applications that are limited by intensity noise and not by available laser power, such as atom trapping.

B. Gaussian and super-Gaussian pulses

1. Intra-pulse relative intensity noise

We now extend our cw analysis to long (nanosecond) pulses with a bandwidth well contained within the phase-matching bandwidth. Since the RIN transfer is time independent, we apply the cw analysis separately for each point in time along the pulse duration. In this section, we adopt a generalized definition of a Gaussian and super-Gaussian temporal intensity profile,

$$I(t) = I_p \exp\left(-2\left(\frac{t}{\tau}\right)^n\right), \tag{11}$$

where I_p is the peak intensity of the input pulse, τ is the pulse duration, and n is a positive even integer. A few examples of such profiles are shown in Fig. 6(c). We refer to the special case of $n = 2$ as a Gaussian pulse.

Figures 4(a) and 4(b) show the $\mathcal{R}_{\mathrm{rms}}$ transfer along a Gaussian pulse for different peak input intensities, for the perturbative and nonperturbative noise case, respectively.

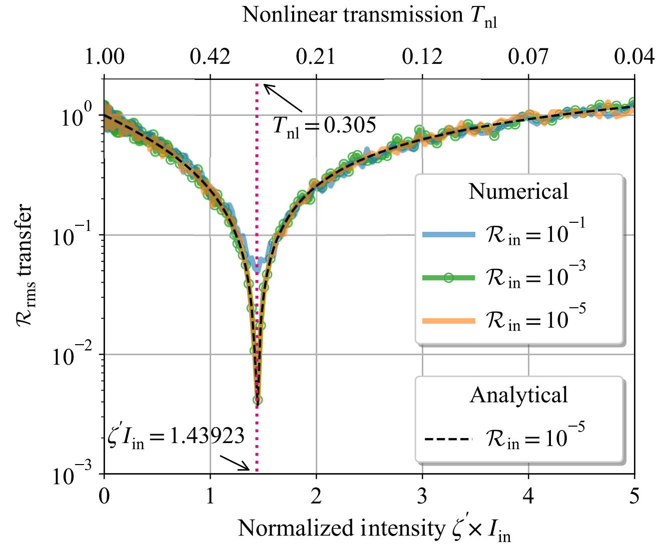

FIG. 3. Analytical and simulated $\mathcal{R}_{\mathrm{rms}}$ transfer for perturbative noise ($\mathcal{R}_{\mathrm{in}} = 10^{-5}$) and simulated $\mathcal{R}_{\mathrm{rms}}$ transfer for both nonperturbative noise ($\mathcal{R}_{\mathrm{in}} = 10^{-1}$) and perturbative noise ($\mathcal{R}_{\mathrm{in}} = 10^{-3}$). The overlapping curves show that the perturbative range extends to $\mathcal{R}_{\mathrm{in}} = 10^{-3}$ and that the analytical formula shows good agreement with the simulated result for perturbative noise.

To underscore the universality of our result, we plot in terms of unitless quantities of normalized time t/τ and normalized intensity $\zeta' \times I_p$. In addition, each plot includes an additional vertical axis showing the nonlinear fluence transmission corresponding to each peak normalized intensity, in order to convey the overall transmission of pulse energy. In both perturbative and nonperturbative cases, the dark green band corresponds to the points in time in which the normalized intensity is close to the critical value, where RIN transfer is lowest. When this point is at the pulse peak ($t = 0$), the overall RIN transfer is lowest, since around the pulse peak the intensity varies most slowly and remains close to the optimal value. For practical applications, it is of greater interest to reduce noise at and around the pulse peak rather than at two short intervals straddling it. Therefore, each figure also includes the curve of $\mathcal{R}_{\mathrm{rms}}$ transfer for this case. Under this optimal condition, the range in which the $\mathcal{R}_{\mathrm{rms}}$ ($\mathcal{R}_f$) attenuation is at least 10 dB encompasses approximately 40% (68%) of the pulse energy for both perturbative and nonperturbative cases, despite the steep slope of the RIN transfer as a function of intensity, and the nonlinear fluence transmission is 44%.

Other applications aiming to increase the utilization of nonlinear interactions have employed nanosecond pulse shaping, e.g., by controlling laser amplifier pump power to generate flat-top pulses [37–39]. Here as well we expect better nonlinear RIN suppression for flat-top pulses where a greater part of the input pulse is at the optimal intensity. Therefore, we repeat the same analysis for rectanglelike super-Gaussian pulses, as shown in Fig. 5. In the

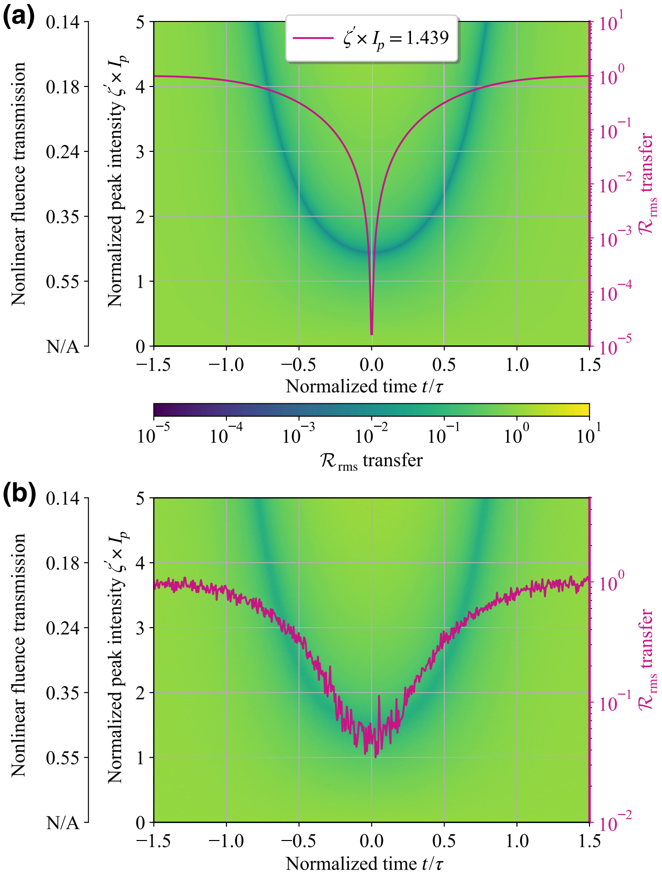

FIG. 4. (a) Perturbative and (b) nonperturbative $\mathcal{R}_{\rm rms}$ noise transfer of pulses with Gaussian profile [$n = 2$ in Eq. (11)]. Each horizontal section represents a pulse of respective peak normalized intensity, with the color corresponding to the intrapulse $\mathcal{R}_{\rm rms}$ transfer. The nonlinear fluence transmission axis refers to the transmission of fluence at the given value of $\zeta' \times I_p$. The location of the troughs at $t = 0$ relates to the intensities of greatest noise attenuation, evaluated in Sec. II. Each subfigure includes a plot of the $\mathcal{R}_{\rm rms}$ transfer along the pulse for the optimal case of $\zeta' I_p = 1.43923$, shown in violet. The simulation in (b) assumes $\mathcal{R}_{\rm rms,in} = 10^{-1}$.

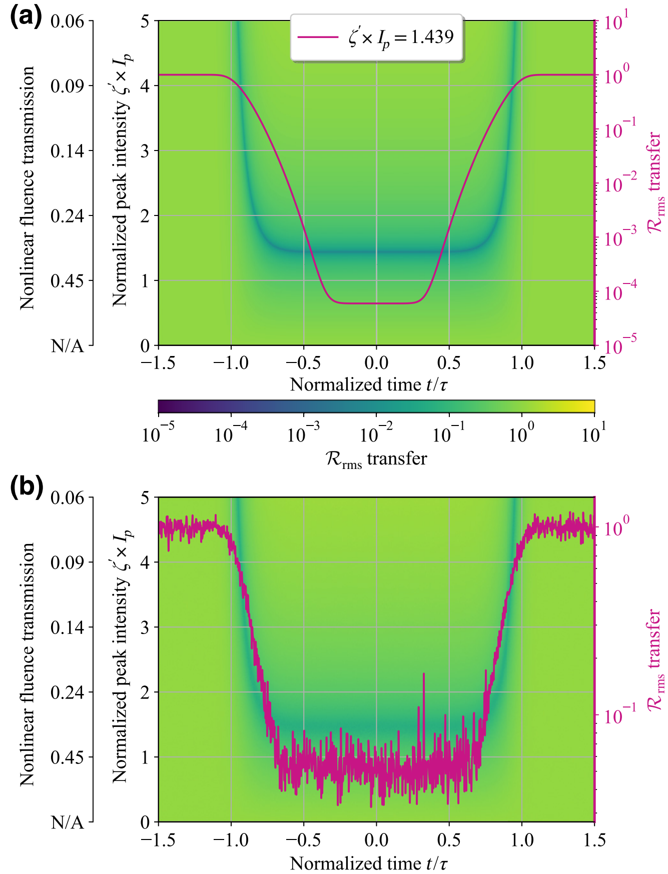

FIG. 5. (a) Perturbative and (b) nonperturbative noise transfer of pulses with super-Gaussian profile, i.e., the same as Fig. 4 for $n = 10$ in Eq. (11). Compared to the Gaussian-shaped pulse of Fig. 4, a greater portion of the pulse receives noise attenuation.

$n = 10$ super-Gaussian example, the 10 dB or greater $\mathcal{R}_{\rm rms}$ ($\mathcal{R}_f$) attenuation region contains 84% (94%) of the pulse energy, for both the perturbative and nonperturbative cases, demonstrating the potential for excellent noise attenuation performance with a well-chosen pulse shape. At the same time, the fluence transmission drops to 33%, owing to the nonlinear transmission being lower for a longer portion of the pulse [see also Fig. 6(d)].

Noting the similarities of the location of the troughs between the perturbative and nonperturbative cases, for both Gaussian and super-Gaussian pulses, one could use the analytical result from the perturbative analysis to select an optimal ζ' (i.e., match a nonlinear crystal to a given laser intensity) even if the noise is nonperturbative.

2. Pulse-to-pulse fluence noise

In addition to intrapulse noise, some applications are very sensitive to pulse-to-pulse energy fluctuations, e.g., material processing [40] or laser-induced breakdown spectroscopy [41]. Many of these applications utilize nanosecond pulses with relatively high pulse energy (mJ–J), that are commonly generated with Q-switched lasers, where higher pulse energy is accompanied by a lower pulse repetition rate (commonly as low as 1 Hz) to avoid detrimental thermal loads due to high average power. However, the decrease in repetition rate leads to a simultaneous increase in pulse-to-pulse energy fluctuations, because the amount of energy buildup in the gain medium depends strongly and nonlinearly on the time interval between pulses, and the absolute error in this time interval is greater when the interval is longer [42]. Consequently, higher pulse energy is accompanied by stronger pulse-to-pulse energy fluctuations.

In this section, we investigate how our proposed scheme damps pulse-to-pulse energy fluctuation in terms of fluence, where fluence is the time integral of intensity, $F =$

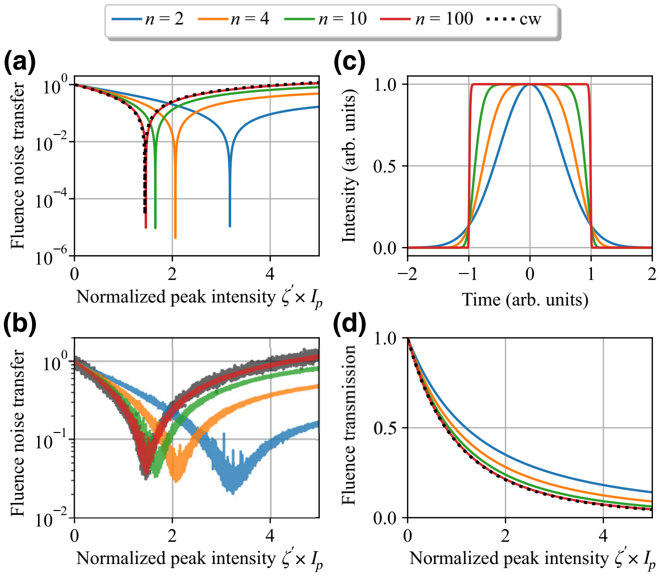

FIG. 6. (a) Perturbative ($\sigma_{F,\mathrm{in}}/\bar{F}_{\mathrm{in}} = 10^{-5}$) and (b) nonperturbative ($\sigma_{F,\mathrm{in}}/\bar{F}_{\mathrm{in}} = 10^{-1}$) fluence noise transfer. For an increasing value of n, the fluence noise attenuation of the super-Gaussian pulse similarly approaches the cw case. (c) Pulse shape and (d) fluence transmission for various orders n of super-Gaussian pulses. The pulse shape becomes rectangular and its fluence transmission approaches the cw case as n increases. Here the pulse duration τ is held constant.

$\int_{\mathrm{pulse}} I(t)\, dt$, and therefore proportional to pulse energy. Similar to the treatment as in Eq. (6), we define the transfer of fluence fluctuation, or fluence noise, as

$$\text{Fluence Noise Transfer} \equiv \frac{\sigma_{F,\mathrm{out}}/\bar{F}_{\mathrm{out}}}{\sigma_{F,\mathrm{in}}/\bar{F}_{\mathrm{in}}}, \tag{12}$$

where σ_F is the rms fluence noise and $\bar{F}$ is the average fluence.

To study the noise attenuation numerically via computer simulations, we devise pulse trains in which the pulse shape is fixed and the peak intensity varies randomly between pulses. Over sufficiently many pulses, the statistics of the input and output fluence converge, which we use to compute the fluence noise transfer as defined in Eq. (12).

Figures 6(a), 6(b), and 6(d) depict the perturbative fluence noise transfer, nonperturbative fluence noise transfer, and fluence transmission, respectively, as functions of the nominal (i.e., noise-free) peak normalized input intensity, for Gaussian and several selected super-Gaussian intensity profiles. Normalized pulse intensity profiles as functions of time are plotted in Fig. 6(c) as a visual aid. For reference, the result for the cw intensity transmission and $\mathcal{R}_{\mathrm{rms}}$ transfer is also shown (dashed black line). For cases shown in Fig. 6(a), the input pulse-to-pulse fluence fluctuations have an rms value of 10^{-5} of the nominal input fluence, i.e., within the perturbative noise regime. For cases shown in Fig. 6(b), the input pulse-to-pulse fluence fluctuations have an rms value of 10^{-1}, which is highly nonperturbative. We expect the pulsed results to approach those of the CW case as n increases and the intrapulse variation in nominal intensity decreases, as is indeed the case for both perturbative and nonperturbative noise. In Fig. 6(d) we see that the fluence transmission is highest for a Gaussian ($n = 2$) pulse, as we explained in Sec. III B 1 when comparing Figs. 4 and 5. For the same reason, Fig. 6(a) reveals a different optimal normalized peak intensity for different pulse shapes (where the fluence noise transfer exhibits a sharp drop towards a single minimum), with the highest optimal $\zeta' I_p$ value belonging to the Gaussian case. Still, for all pulse shapes, the optimal fluence noise attenuation is at least 50 dB for perturbative noise and 15 dB for nonperturbative noise, again limited by our numerical precision.

It is worth noting that the optimal peak normalized intensity for RIN attenuation (i.e. $\zeta' I_p = 1.43923$) does not necessarily coincide with that for fluence noise attenuation. As the value of n grows and the pulse shape gradually becomes rectangular [as shown in Figs. 6(a) and 6(c)], the optimum for fluence noise attenuation approaches the optimum for RIN attenuation. Moreover, the comparison between Figs. 6(a) and 6(b) shows that this trend holds regardless of whether the noise is perturbative or not. Empirically, we found two functions that describe the position of the minima in Fig. 6(a):

$$\zeta' \times I_p(n) = 1.43923 \times (1.504 \times \pi)^{1/n}, \tag{13a}$$

$$\zeta' \times I_p(n) = 3.61 n^{-2} + 1.65 n^{-1} + 1.44. \tag{13b}$$

The shape of the hyperbolic function with $\zeta' I_p(2) \approx \pi$ and $\zeta' I_p(n \to \infty) = 1.43923$ inspires the form of Eq. (13a), whereas a straightforward polynomial fit produces Eq. (13b). These two functions are plotted in Figs. 7(a) and 7(b). Both functions yield practical guidance on selecting a nonlinear medium and focusing conditions for a given pulse shape and pulse energy.

3. Pulse shape variation

Since the nonlinear transmission is intensity-dependent, the transmitted pulse shape differs from that of the input. To quantify this variation, we consider the zero-delay cross-correlation between the input and output pulse shapes relative to the autocorrelation of the input pulse shape,

$$\eta = \frac{\int \tilde{I}_{\mathrm{in}}(t) \tilde{I}_{\mathrm{out}}(t)\, dt}{\int \tilde{I}_{\mathrm{in}}^2(t)\, dt}, \tag{14}$$

where $\tilde{I}_{\mathrm{in}}(t) = \tau \times I_{\mathrm{in}}(t)/F_{\mathrm{in}}$ and $\tilde{I}_{\mathrm{out}}(t) = \tau \times I_{\mathrm{out}}(t)/F_{\mathrm{out}}$ are the input and output pulse intensities normalized by

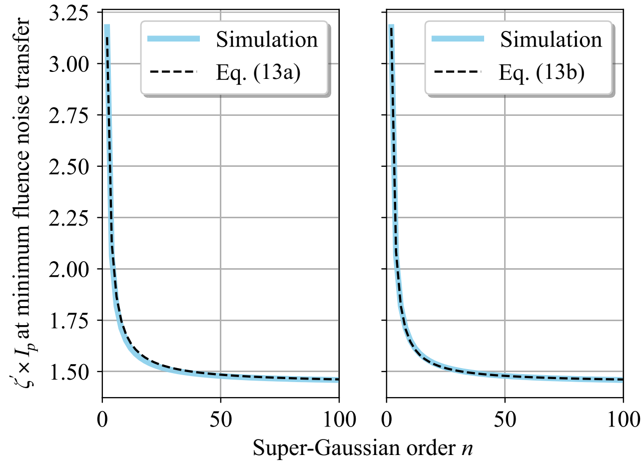

FIG. 7. Comparison of Eq. (13) with respect to simulated result indicates good fit. Either of the functions may be used for the practical choice of ζ' for a given peak intensity.

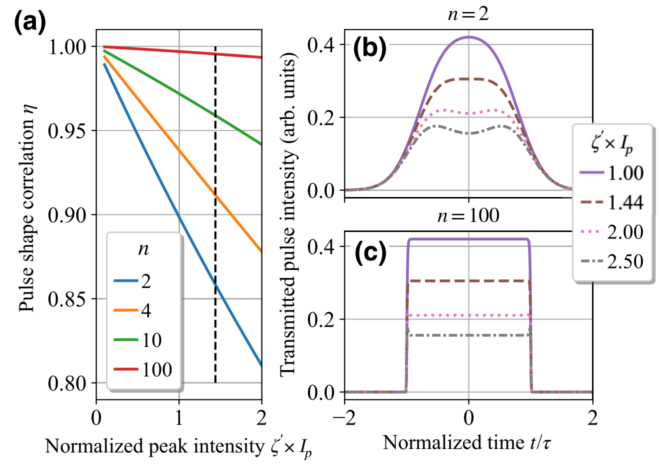

FIG. 8. Pulse-shape variation quantified (a) via pulse-shape correlation for different super-Gaussian orders n as a function of normalized peak intensity, and demonstrated for output pulses obtained from (b) Gaussian ($n = 2$) and (c) super-Gaussian ($n = 100$) input pulses with different values of normalized peak intensity. In (a), the dashed line indicates the optimum normalized peak intensity value of 1.43923.

their respective average intensities. The pulse-shape correlation η is a unitless quantity that ranges between 0 and 1, where a value close to zero indicates significant dissimilarities between the input and output pulse shapes and a value close to unity indicates negligible pulse-shape variation.

Figure 8(a) shows pulse-shape correlation values for different orders of super-Gaussian pulses as a function of normalized peak intensity. Evidently, η increases with super-Gaussian order n, for the same normalized peak intensity. The reason behind this trend is the intensity dependence of the nonlinear transmission, which translates into a variation in transmission along the pulse.

Figures 8(b) and 8(c) illustrate the effects of such variation by plotting the transmitted super-Gaussian pulses ($n = 2$ and $n = 100$, respectively) at various normalized intensities. For the $n = 2$ case, the variation falls into three regimes, qualitatively. When the input peak intensity is small compared to the optimum ($\zeta' \times I_p < 1.43923$), the nonlinear interaction is weak and the variation is not pronounced; when the input peak intensity is close to optimum ($\zeta' \times I_p \approx 1.43923$), the variation "flattens" the pulse peak since the nonlinear transmission counteracts against the change of intensity near this optimum (see Fig. 1); when the input peak intensity is large compared to the optimum ($\zeta' \times I_p > 1.43923$), the transmitted pulse loses its singular peak due to the low nonlinear transmission at high intensities. For the case of $n = 100$ as in Fig. 8(c), where intensity is constant throughout the pulse duration, the variation is minor, and it manifests as small undershoots and overshoots near the rising and falling edges. Overall, for peak intensities up to the optimum value, all considered pulse shapes remain single peaked and the pulse-shape correlation exceeds 0.85, indicating a small degree of variation that is acceptable for almost all applications.

C. Asymmetrical pulses

1. Intrapulse relative intensity noise

Some strongly pumped Q-switched lasers produce asymmetric pulse shapes, with a fast-rising leading edge (due to the high amount of energy stored in the gain medium) followed by a more slowly falling trailing edge (due to low cavity loss) [43]. We analyze our method's performance with such pulses, which we model as two halves of a Gaussian pulse, each with a different time constant,

$$I(t) = \begin{cases} I_p \exp\left(-2\left(\frac{t}{a\tau}\right)^2\right) & t < 0 \\ I_p \exp\left(-2\left(\frac{t}{\tau}\right)^2\right) & t \geq 0 \end{cases}, \tag{15}$$

where $0 < a \leq 1$ is an arbitrary constant, modeling the pulse asymmetry. The numerical result calculated using Eq. (10) is shown in Fig. 9, and selected asymmetrical pulse shapes are shown in Fig. 10(c). To draw a meaningful comparison between asymmetrical pulse and Gaussian pulse, we again present the result in the normalized time unit of t/τ, where the decay rate τ is kept constant across all simulations to preserve generality. In this example, the faster growth rate of the leading edge causes the intensity to quickly deviate from the optimum RIN attenuation intensity, resulting in a degraded performance compared to the cases of Gaussian and super-Gaussian pulses. In Fig. 9, the violet curve of RIN transfer function at $\zeta' I_p = 1.43923$ demonstrates that a narrower region in time benefits from the noise attenuation effect. Indeed, the region where $\mathcal{R}_{\rm rms}$ attenuation is at least 10 dB contains

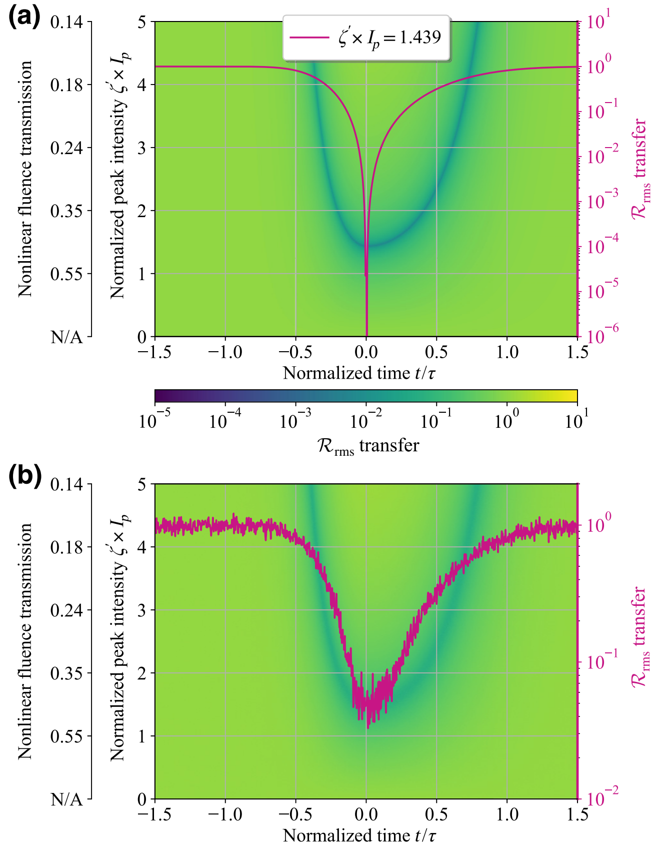

FIG. 9. (a) Perturbative and (b) nonperturbative noise transfer of pulses with asymmetrical profile, i.e., the same as Fig. 4 for $a = 0.5$ in Eq. (15).

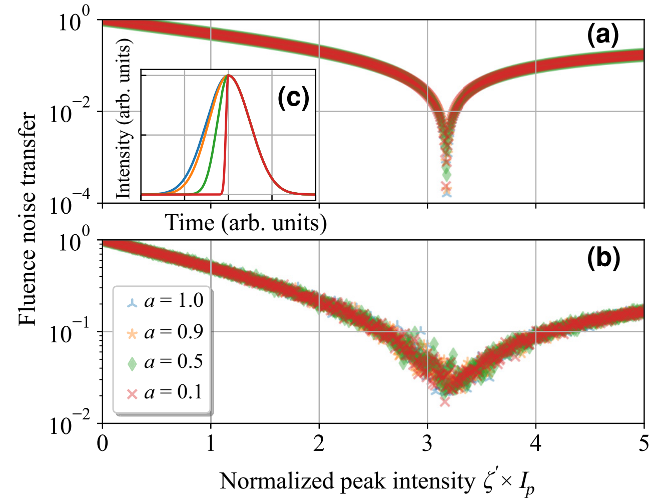

FIG. 10. (a) Perturbative ($\sigma_{F,\rm in}/\bar{F}_{\rm in} = 10^{-5}$) and (b) nonperturbative ($\sigma_{F,\rm in}/\bar{F}_{\rm in} = 10^{-1}$) fluence noise transfer for selected asymmetrical pulse shapes, parameterized by the value of a in Eq. (15), as a function of peak normalized intensity. The inset (c) shows the effect of the parameter a on the pulse-shape asymmetry. The overlapping data points in both (a),(b) show that the fluence noise attenuation is independent of the degree of asymmetry. The comparison between (a),(b) shows that whether or not the noise is perturbative does not change the optimal $\zeta' \times I_p$ value for fluence noise attenuation.

only 20% of the pulse energy, for both the perturbative and nonperturbative noise cases.

2. Pulse-to-pulse fluence noise

As explained above, pulse asymmetry is more pronounced in strongly-pumped Q-switched lasers, where pulse energy is high and repetition rate is low, which also produces greater pulse-to-pulse energy fluctuations as outlined in Sec. III B 2. Therefore, we now examine the impact of pulse asymmetry on fluence noise transfer.

Figures 10(a) and 10(b) show perturbative and nonperturbative fluence noise transfer, respectively, for different values of the asymmetry parameter a. For all values of a, the numerically calculated data points overlap, showing that pulse asymmetry does not impact the fluence noise attenuation. Pulse-to-pulse fluence fluctuation is attenuated by at least 36 dB for perturbative noise and 17 dB for nonperturbative noise regardless of asymmetry, while the calculation of these values is limited by our numerical precision (i.e., actual noise suppression may be higher). We note that, as in the case for symmetric Gaussian pulses, the optimal normalized peak intensity for RIN attenuation is different from the one for pulse-to-pulse noise attenuation and that whether or not the noise is perturbative does not change the optimum $\zeta' \times I_p$ value for fluence noise attenuation.

IV. CONCLUSION

To summarize, we have theoretically modeled and numerically simulated a broadband intensity noise and pulse-to-pulse energy fluctuation (i.e., fluence noise) attenuation method based on an SHG process, where noise is attenuated for the fundamental frequency wave. This method utilizes only passive components, thus avoiding the complexity and out-of-band noise increase (“servo bump”) of feedback-based approaches. Here, the noise-attenuation mechanism depends exclusively on intensity and is consequently independent of the noise spectrum, allowing uniform RIN attenuation at frequencies that are outside the reach of conventional noise eaters.

Through perturbative analysis, we found that the strongest intensity noise attenuation occurs when $\zeta' \times I_{\rm in} = 1.43923$. To validate our result, we have numerically simulated the noise attenuation performance, for both perturbative and nonperturbative noise, for cw lasers and pulsed lasers with various pulse shapes. For cw lasers, we numerically demonstrated $\mathcal{R}_{\rm rms}$ ($\mathcal{R}_f$) suppression as high as 24 dB (48 dB) for perturbative noise, and 13 dB (26 dB) for very strong noise of 10% of rms intensity. These findings make this an excellent method for greatly increasing atom trap storage time, which is often significantly limited by laser intensity noise. Among Gaussian, super-Gaussian, and asymmetrical Gaussian pulses, the optimal pulse-to-pulse fluence fluctuation suppression is the same for all pulse shapes at about 50 dB. However, the optimal peak intensities for attenuating pulse-to-pulse fluence fluctuations and intrapulse intensity noise could differ, depending on the pulse shape. We discovered that high-order super-Gaussian pulse shapes experience the least pulse-shape variation and benefit the most in concurrent intrapulse RIN and pulse-to-pulse fluence noise attenuation.

Finally, we note that here we limited our analysis to loosely focused narrowband light sources, such that the SHG phase-matching bandwidth exceeds the angular and optical bandwidth. However, our method could be extended to broadband sources, such as femtosecond lasers, by considering methods for broadband phase matching, e.g., adiabatic frequency conversion [44–47], random quasi-phase-matching [48], or composite segment schemes [49].

ACKNOWLEDGMENTS

We acknowledge the support of the Natural Sciences and Engineering Research Council of Canada (NSERC), [funding reference number RGPIN-2019-05017], the Government of Canada's New Frontiers in Research Fund (NFRF), [NFRFE-2018-01220], NSERC Alliance-Alberta Innovates Advance [570922-21 and 212200789], Quantum Major Innovation Fund Project [RCP-19-004-MIF], and Quantum City [1059845-10]. Additionally, the authors would like to thank Saeid Ebrahimzadeh and Campbell Rea for helpful discussions.

[1] I. Coto Hernàndez, M. d'Amora, A. Diaspro, and G. Vicidomini, Influence of laser intensity noise on gated CW-STED microscopy, Laser Phys. Lett. **11**, 095603 (2014).

[2] K. Somiya, Y. Chen, S. Kawamura, and N. Mio, Frequency noise and intensity noise of next-generation gravitational-wave detectors with RF/DC readout schemes, Phys. Rev. D **73**, 122005 (2006).

[3] T. Mikkonen, G. Genty, and J. Toivonen, Supercontinuum intensity noise coupling in Fourier transform photoacoustic spectroscopy, Opt. Lett. **47**, 1713 (2022).

[4] M. E. Gehm, K. M. O'Hara, T. A. Savard, and J. E. Thomas, Dynamics of noise-induced heating in atom traps, Phys. Rev. A **58**, 3914 (1998).

[5] T. A. Savard, K. M. O'Hara, and J. E. Thomas, Laser-noise-induced heating in far-off resonance optical traps, Phys. Rev. A **56**, R1095 (1997).

[6] S. Blatt, A. Mazurenko, M. F. Parsons, C. S. Chiu, F. Huber, and M. Greiner, Low-noise optical lattices for ultracold ^{6}Li, Phys. Rev. A **92**, 021402 (2015).

[7] R. Grimm, M. Weidemüller, and Y. B. Ovchinnikov, *Optical Dipole Traps for Neutral Atoms*, edited by B. Bederson and H. Walther (Academic Press, San Diego, 2000), Vol. 42, pp. 95–170.

[8] T. Schaetz, Trapping ions and atoms optically, J. Phys. B: At. Mol. Opt. Phys. **50**, 102001 (2017).

[9] A. Mosk, S. Jochim, H. Moritz, T. Elsässer, M. Weidemüller, and R. Grimm, Resonator-enhanced optical dipole trap for fermionic lithium atoms, Opt. Lett. **26**, 1837 (2001).

[10] B. C. Buchler, E. H. Huntington, C. C. Harb, and T. C. Ralph, Feedback control of laser intensity noise, Phys. Rev. A **57**, 1286 (1998).

[11] Y. Wang, K. Wang, E. F. Fenton, Y.-W. Lin, K.-K. Ni, and J. D. Hood, Reduction of laser intensity noise over 1 MHz band for single atom trapping, Opt. Express **28**, 31209 (2020).

[12] Q. Zhao, S. Xu, K. Zhou, C. Yang, C. Li, Z. Feng, M. Peng, H. Deng, and Z. Yang, Broad-bandwidth near-shot-noise-limited intensity noise suppression of a single-frequency fiber laser, Opt. Lett. **41**, 1333 (2016).

[13] E. Ivanov, Wide-band suppression of laser intensity noise, IEEE Trans. Ultrason., Ferroelect., Freq. Contr. **56**, 22 (2009).

[14] E. A. Michael and L. Pallanca, Broadband near-to-shot-noise suppression of arbitrary cw-laser excess intensity noise in the gigahertz range, Opt. Lett. **40**, 1334 (2015).

[15] L. Li, W. Huie, N. Chen, B. DeMarco, and J. P. Covey, Active cancellation of servo-induced noise on stabilized lasers via feedforward, Phys. Rev. Appl. **18**, 064005 (2022).

[16] K. Inoue and T. Mukai, Experimental study on noise characteristics of a gain-saturated fiber optical parametric amplifier, J. Lightwave Technol. **20**, 969 (2002).

[17] S. Matsuo, L. Yan, J. Si, T. Tomita, and S. Hashimoto, Reduction of pulse-to-pulse fluctuation in laser pulse energy using the optical Kerr effect, Opt. Lett. **37**, 1646 (2012).

[18] S. Di Fonzo, P. Mataloni, and S. Bollanti, Laser power stabilization by means of internal second harmonic generation, Opt. Commun. **71**, 295 (1989).

[19] H. Lu, Y. Guo, and K. Peng, Intensity noise manipulation of a single-frequency laser with high output power by intracavity nonlinear loss, Opt. Lett. **40**, 5196 (2015).

[20] K. Audo and M. Alouini, Intensity noise cancellation in solid-state laser at 1.5 μm using SHG depletion as a buffer reservoir, Appl. Opt. **57**, 1524 (2018).

[21] T. Harimoto and H. Tsugane, Peak intensity stabilization of fundamental laser through second-harmonic generation process, Jpn. J. Appl. Phys. **51**, 088002 (2012).

[22] J. A. Armstrong, N. Bloembergen, J. Ducuing, and P. S. Pershan, Interactions between light waves in a nonlinear dielectric, Phys. Rev. **127**, 1918 (1962).

[23] R. W. Boyd, *Nonlinear Optics* (Academic Press, Burlington, 2008), 3rd ed.

[24] C. Dixneuf, G. Guiraud, H. Ye, Y.-V. Bardin, M. Goeppner, G. Santarelli, and N. Traynor, Robust 17 W single-pass second-harmonic-generation at 532 nm and relative-intensity-noise investigation, Opt. Lett. **46**, 408 (2021).
[25] U. Keller, *Ultrafast Lasers* (Springer, Cham, 2021).
[26] H. H. Ku, Notes on the use of propagation of error formulas, J. Res. Natl. Bur. Stand. **70**, 263 (1966).
[27] O. Gayer, Z. Sacks, E. Galun, and A. Arie, Temperature and wavelength dependent refractive index equations for MgO-doped congruent and stoichiometric $LiNbO_3$, Appl. Phys. B **91**, 343 (2008).
[28] D. N. Nikogosyan, *Nonlinear Optical Crystals: A Complete Survey* (Springer Science+Business Media, New York, 2005).
[29] K. Devi, S. Parsa, and M. Ebrahim-Zadeh, Continuous-wave, single-pass, single-frequency second-harmonic-generation at 266 nm based on birefringent-multicrystal scheme, Opt. Express **24**, 8763 (2016).
[30] T. Harimoto, B. Yo, and K. Uchida, A novel multipass scheme for enhancement of second harmonic generation, Opt. Express **19**, 22692 (2011).
[31] I. Ricciardi, M. De Rosa, A. Rocco, P. Ferraro, and P. De Natale, Cavity-enhanced generation of 6 W cw second-harmonic power at 532 nm in periodically-poled MgO : $LiTaO_3$, Opt. Express **18**, 10985 (2010).
[32] G. Marschick, J. Pelini, T. Gabbrielli, F. Cappelli, R. Weih, H. Knötig, J. Koeth, S. Höfling, P. De Natale, G. Strasser, S. Borri, and B. Hinkov, Mid-infrared ring interband cascade laser: Operation at the standard quantum limit, ACS. Photonics **11**, 395 (2024).
[33] G. Bloom, A. Grisard, E. Lallier, C. Larat, M. Carras, and X. Marcadet, Optical parametric amplification of a distributed-feedback quantum-cascade laser in orientation-patterned GaAs, Opt. Lett. **35**, 505 (2010).
[34] Q. Clément, J.-M. Melkonian, J. Barrientos-Barria, J.-B. Dherbecourt, M. Raybaut, and A. Godard, Tunable optical parametric amplification of a single-frequency quantum cascade laser around 8 μm in $ZnGeP_2$, Opt. Lett. **38**, 4046 (2013).
[35] C. R. Harris, *et al.*, Array programming with NumPy, Nature **585**, 357 (2020).
[36] J. D. Hunter, Matplotlib: A 2D graphics environment, Comput. Sci. Eng. **9**, 90 (2007).
[37] Z. Sacks, O. Gayer, E. Tal, and A. Arie, Improving the efficiency of an optical parametric oscillator by tailoring the pump pulse shape, Opt. Express **18**, 12669 (2010).
[38] K. T. Vu, A. Malinowski, D. J. Richardson, F. Ghiringhelli, L. M. B. Hickey, and M. N. Zervas, Adaptive pulse shape control in a diode-seeded nanosecond fiber MOPA system, Opt. Express **14**, 10996 (2006).
[39] Y. Shen, S.-u. Alam, K. Kang Chen, D. Lin, S. Cai, B. Wu, P. Jiang, A. Malinowski, and D. J. Richardson, PPMgLN-based high-power optical parametric oscillator pumped by Yb^{3+}-doped fiber amplifier incorporates active pulse shaping, IEEE J. Sel. Top. Quantum Electron. **15**, 385 (2009).
[40] W. M. Steen and J. Mazumder, *Laser Material Processing* (Springer Science & Business Media, London, 2010), 4th ed.
[41] J. Singh, J. Almirall, M. Sabsabi, and A. Miziolek, Laser-induced breakdown spectroscopy (LIBS), Anal. Bioanal. Chem. **400**, 3191 (2011).
[42] A. Sennaroglu, *Solid-State Lasers and Applications* (CRC Press, Boca Raton, 2007).
[43] A. E. Siegman, *Lasers* (University Science Books, Sausalito, 1986).
[44] H. Suchowski, G. Porat, and A. Arie, Adiabatic processes in frequency conversion, Laser. Photon. Rev. **8**, 333 (2014).
[45] E. Bahar, X. Ding, A. Dahan, H. Suchowski, and J. Moses, Adiabatic four-wave mixing frequency conversion, Opt. Express **26**, 25582 (2018).
[46] X. Ding, D. Heberle, K. Harrington, N. Flemens, W.-Z. Chang, T. A. Birks, and J. Moses, Observation of rapid adiabatic passage in optical four-wave mixing, Phys. Rev. Lett. **124**, 153902 (2020).
[47] P. Margules, J. Moses, H. Suchowski, and G. Porat, Ultrafast adiabatic frequency conversion, J. Phys.: Photonics **3**, 022011 (2021).
[48] M. Baudrier-Raybaut, R. Haïdar, P. Kupecek, P. Lemasson, and E. Rosencher, Random quasi-phase-matching in bulk polycrystalline isotropic nonlinear materials, Nature **432**, 374 (2004).
[49] Y. Erlich, A. Rangelov, G. Montemezzani, and H. Suchowski, Robust, efficient, and broadband SHG of ultrashort pulses in composite crystals, Opt. Lett. **44**, 3837 (2019).